Editors' Suggestion

Differing vibrational properties of halide and chalcogenide perovskite semiconductors and impact on optoelectronic performance

Kevin Ye [1,*] Matan Menahem [2,*] Tommaso Salzillo [3] Florian Knoop [4] Boyang Zhao [5] Shanyuan Niu [5] Olle Hellman [4,6] Jayakanth Ravichandran [5,7,8] R. Jaramillo [1,†] and Omer Yaffe [2,‡]

[1]*Department of Materials Science and Engineering, Massachusetts Institute of Technology, Cambridge, Massachusetts 02139, USA*
[2]*Department of Chemical and Biological Physics, Weizmann Institute of Science, Rehovot 76100, Israel*
[3]*Department of Industrial Chemistry "Toso Montanari", INSTM-UdR Bologna, Bologna 40129, Italy*
[4]*Department of Physics, Chemistry and Biology (IFM), Linköping University, SE-581 83, Linköping, Sweden*
[5]*Mork Family Department of Chemical Engineering and Materials Science, University of Southern California, Los Angeles, California 90089, USA*
[6]*Department of Molecular Chemistry and Material Science, Weizmann Institute of Science, Rehovot 76100, Israel*
[7]*Ming Hsieh Department of Electrical and Computer Engineering, University of Southern California, Los Angeles, California 90089, USA*
[8]*Core Center of Excellence in NanoImaging (CNI), University of Southern California, Los Angeles, California 90089, USA*

(Received 14 April 2024; revised 23 June 2024; accepted 3 July 2024; published 20 August 2024)

We report a comparative study of temperature-dependent photoluminescence and structural dynamics of two perovskite semiconductors, the chalcogenide $BaZrS_3$ and the halide $CsPbBr_3$. These materials have similar crystal structures and direct band gaps, but we find that they have quite distinct optoelectronic and vibrational properties. Both materials exhibit thermally activated nonradiative recombination, but the nonradiative recombination rate in $BaZrS_3$ is four orders of magnitude faster than in $CsPbBr_3$, for the crystals studied here. Raman spectroscopy reveals that the effects of phonon anharmonicity are far more pronounced in $CsPbBr_3$ than in $BaZrS_3$. Further, although both materials feature a large dielectric response due to low-energy polar optical phonons, the phonons in $CsPbBr_3$ are substantially lower in energy than in $BaZrS_3$. Our results suggest that electron-phonon coupling in $BaZrS_3$ is more effective at nonradiative recombination than in $CsPbBr_3$ and that $BaZrS_3$ may also have a substantially higher concentration of nonradiative recombination centers than $CsPbBr_3$. The low defect concentration in $CsPbBr_3$ may be related to the ease of lattice reconfiguration, typified by anharmonic bonding. It remains to be seen to what extent these differences are inherent to the chalcogenide and halide perovskites and to what extent they can be affected by materials processing.

DOI: 10.1103/PhysRevMaterials.8.085402

I. INTRODUCTION

Halide perovskites exhibit outstanding optoelectronic properties and are under intensive development for photovoltaic (PV) applications [1–3]. These materials can be synthesized at near-room temperature and feature sharp band-edge optical absorption and long excited-state charge carrier lifetimes [4–8]. However, halide perovskites suffer from thermal and chemical instability, as well as lead toxicity, and research continues into alternative materials for thin-film photovoltaics. Chalcogenide perovskites are an intriguing alternative. This class of materials possesses a similar crystal structure and range of direct band gaps as their halide counterparts [9–11]. Additionally, chalcogenide perovskites have a very large dielectric constant, suggesting similar lattice dynamics and screening of charged defects [12,13]. However, despite these similarities, chalcogenide and halide perovskites are quite different in other respects. Chalcogenide perovskites are made from Earth-abundant elements and present minimal toxicity concerns. Their synthesis is challenging, typically requiring very high temperatures and air-free processing. Once formed, chalcogenide perovskites are very stable [9,14–17]. The optoelectronic properties of chalcogenide perovskites have been little reported. Existing published results suggest that photoluminescence (PL) is not strong, and defect control remains a challenge, but long PL transient decay times have been measured [9,16–21]. No chalcogenide perovskite thin-film solar cells have been reported, likely due to the challenging conditions required for film synthesis.

Many researchers, including ourselves, have argued that the outstanding optoelectronic properties of halide perovskites are intertwined with their strongly anharmonic structural dynamics [22–31]. This poses questions of how the optoelectronic properties and lattice dynamics of chalcogenide and halide perovskites compare and what we can learn about photovoltaic performance from this comparison.

Here, we employ temperature-dependent PL and Raman scattering spectroscopy, alongside first-principles self-consistent phonons simulations, to compare single-crystal samples of two prototypical perovskite semiconductors: the chalcogenide $BaZrS_3$ and the halide $CsPbBr_3$. These compounds share the same distorted-perovskite, corner-sharing, orthorhombic crystal structure (space group *Pnma*, no. 62)

*These authors contributed equally to this work.
†Contact author: rjaramil@mit.edu
‡Contact author: omer.yaffe@weizmann.ac.il

within the temperature range studied here [32,33]. $BaZrS_3$ is the most widely studied chalcogenide perovskite, and has been experimentally made and measured in various form factors [9,12–21,32,34–38]. $CsPbBr_3$ is among the most widely studied inorganic halide perovskite [39–43]. It has a band gap comparable to $BaZrS_3$ and it can be prepared as high-quality single crystals [44–49].

Between 80 and 300 K, the PL emission intensity of both materials decreases due to thermally activated nonradiative recombination, with electron-phonon interactions broadening the PL linewidth in both cases. However, $CsPbBr_3$ emission intensity surpasses that of $BaZrS_3$ by over four orders of magnitude, suggesting a significantly higher concentration of very-low-barrier nonradiative recombination centers in $BaZrS_3$.

We use Raman spectroscopy and first-principles simulations to show that the phonon frequency spectrum in $BaZrS_3$ extends to nearly double that in $CsPbBr_3$. Raman analysis demonstrates that $CsPbBr_3$ exhibits pronounced anharmonic characteristics, even at low temperatures. In contrast, $BaZrS_3$ exhibits predominantly harmonic vibrational behavior akin to traditional tetrahedrally bonded semiconductors. Our findings are consistent with the hypotheses that the lower-frequency and strongly anharmonic structural dynamics in $CsPbBr_3$ may reduce carrier capture cross-sections due to Franck-Condon effects [50]. They may also decrease defect concentration through annealing, even at room temperature [51]. Definitive tests of these hypotheses await detailed calculations of rate coefficients, supported by first-principles quantum calculations and defect spectroscopy to identify and quantify recombination-active defects experimentally.

II. METHODS

We grew single crystals of $BaZrS_3$ with dimensions of approximately 100 μm using a flux method as reported previously [9]. We grew single crystals of $CsPbBr_3$ with dimensions on the order of 2 mm using the vapor saturation of an antisolvent method as reported previously [44].

We performed Raman scattering in a homebuilt system in backscattering geometry. We used a 1.58 eV CW pump-diode laser (Toptica Inc., USA), which is below the band gap of $BaZrS_3$ (1.9 eV) [9,34] and $CsPbBr_3$ (2.32 eV) [52]. We performed PL spectroscopy using the same optical system and a 2.54 eV CW sapphire-pumped diode laser (Coherent Inc., USA). The signal was measured in a 1 m long spectrometer (FHR1000, Horiba Inc.) equipped with a holographic grating (1800 gr/mm for Raman and 150 gr/mm for PL) and a Synapse Plus CCD detector (Horiba Inc.).

We controlled the sample temperature using a liquid N_2- or liquid He-cooled high-vacuum optical cryostat (Janis Inc., USA) for $T \leqslant 400$ K. For higher temperature measurements, we controlled the temperature in an optical furnace (Linkam TS1000) under N_2 flow. We performed measurements for a series of increasing temperatures. We took precautions to isolate the effect of varying sample temperature on the measured spectra by maintaining stable measurement conditions, refocusing the laser before every measurement, and taking repeated measurements across the whole temperature range. We verified sample integrity by the repeatability of the measured spectra and by optical microscope inspection after each measurement sequence. We did not observe evidence of sample damage [53,54], except when the $BaZrS_3$ sample was heated to 850 K (consistent with reported thermal stability to at least 600 °C). [14] The measurement system and protocols are further described in Refs. [55–59].

We calculate normalized PL yield (Y) by analyzing the integrated PL intensity, including both the band-to-band peaks and the shoulders. The PL data is measured in counts, and we compute intensity by dividing by the acquisition time. We define Y as the ratio between the PL intensity emitted from the sample (I_{PL}, measured in counts/sec) and the excitation laser intensity that reaches the interior of the sample (I_{in}):

$$Y = \frac{I_{\mathrm{PL}}}{I_{\mathrm{in}}} = \frac{I_{\mathrm{PL}}}{I_0}(1 - R_{\mathrm{s}})^{-1}. \tag{1}$$

We measure the laser intensity I_0 (in photons/sec) at the microscope entrance. We compute I_{in} from I_0 by accounting for losses due to reflection from the cryostat windows and the sample surface. The same cryostat window reflection losses affect the collected PL intensity and cancel in the expression for Y, leaving only a dependence on the sample surface power reflection coefficient (R_{s}). Further details are presented in Sec. S1 of the Supplemental Material (SM) [60].

III. RESULTS

A. Photoluminescence and nonradiative recombination

In Fig. 1, we present temperature-dependent PL spectra of $BaZrS_3$ and $CsPbBr_3$ measured between 80–300 K. At low temperatures, the spectra are dominated by band-edge recombination at $E_g \approx 1.96$ eV and 2.34 eV for $BaZrS_3$ and $CsPbBr_3$, respectively. The low-temperature spectra for both samples feature low-energy shoulders, which are quenched at elevated temperatures. The band-to-band peak and the shoulder are much broader in $BaZrS_3$ than in $CsPbBr_3$. In both materials, PL is quenched with increasing temperature, and for $BaZrS_3$, it becomes too weak to measure above 170 K. To eliminate external features in the PL spectra, the high-temperature spectra were subtracted from those in Fig. 1.

$BaZrS_3$ and $CsPbBr_3$ are direct band-gap semiconductors and strongly absorb the pump laser. At the pump laser energy of 2.54 eV, the absorption coefficient of $BaZrS_3$ is $1.68 \times 10^5\ \mathrm{cm}^{-1}$, and that of $CsPbBr_3$ is $4.04 \times 10^5\ \mathrm{cm}^{-1}$ [37,61,62]. Therefore, the pump laser absorption depth is much smaller than the thickness for both single-crystal samples, and all the light entering the samples is absorbed. However, the PL emission intensity of $CsPbBr_3$ dwarfs that of $BaZrS_3$.

In Fig. 2(a), we present an Arrhenius plot of the normalized PL yield (Y) of the main band-to-band transition (deconvolution detailed in Sec. S1 of the SM [60]). We fit the data to a minimal model of thermally activated nonradiative recombination [63,64]:

$$Y(T) = \frac{1}{1 + Ae^{-E_{\mathrm{a}}/k_{\mathrm{B}}T} + Be^{-E_{\mathrm{b}}/k_{\mathrm{B}}T}}, \tag{2}$$

where E_{a} and E_{b} are the activation energies of two nonradiative recombination mechanisms, k_B is the Boltzmann constant, and T is the temperature. $A = k^0_{\mathrm{nr,a}}/k_{\mathrm{r}}$ and $B = k^0_{\mathrm{nr,b}}/k_{\mathrm{r}}$ are ratios of exponential prefactors that compare the nonradiative

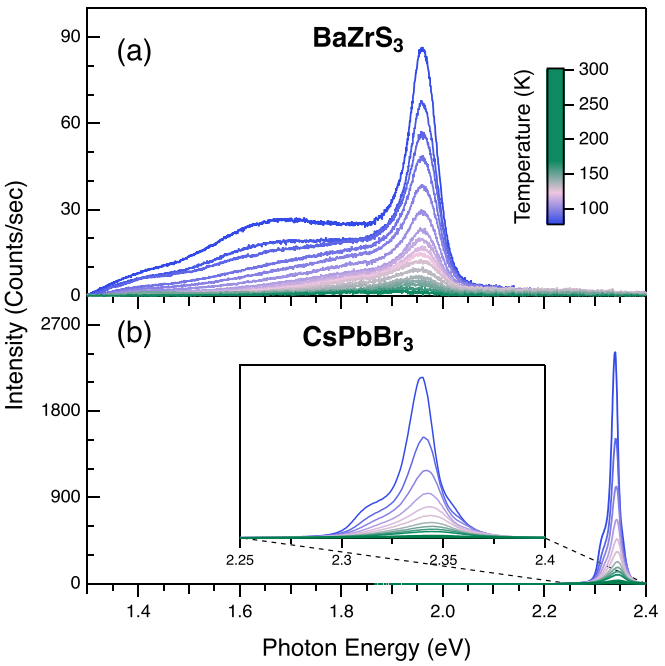

FIG. 1. Temperature-dependent PL spectra. PL spectra measured between 80 K and 300 K for (a) $BaZrS_3$ and (b) $CsPbBr_3$, after subtraction of the background spectra at 170 K and 300 K, respectively. The line color indicates temperature. $BaZrS_3$ and $CsPbBr_3$ were measured with different pump laser fluence: 4.3 MJ/cm^2 for $BaZrS_3$, and 2.7×10^{-4} MJ/cm^2 for $CsPbBr_3$.

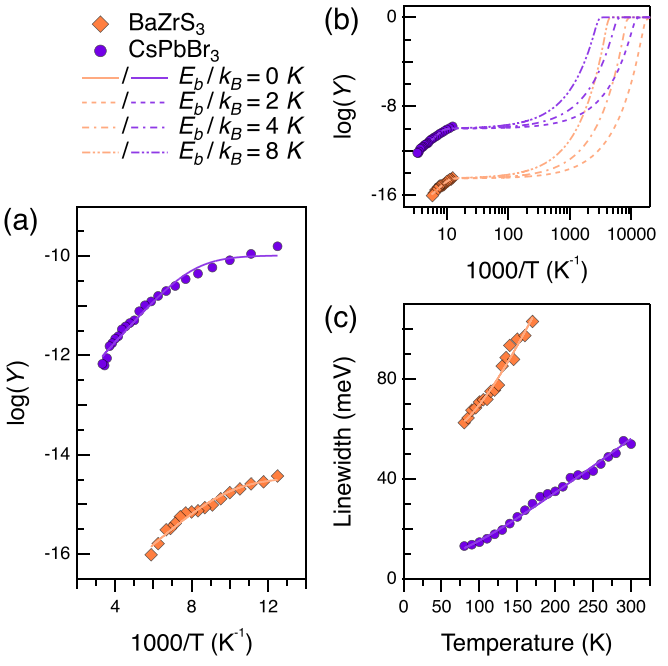

FIG. 2. Model-based analysis of normalized PL yield [Y, Eq. (2)] and linewidth (Γ_{PL}). (a) Y as a function of the inverse temperature. (b) Fit to a model with a second nonradiative recombination pathway. E_b/k_B fall below our measurement temperature window. (c) Γ_{PL} of the band-to-band peak as a function of the temperature. All fitted values can be found in Sec. S1 of the SM [60]. Purple circles and traces are for $CsPbBr_3$, orange diamonds and traces are for $BaZrS_3$.

($k^0_{nr,a}$ and $k^0_{nr,b}$) to radiative (k_r) recombination rate coefficients at $T = 0$ K. As discussed below, two nonradiative recombination mechanisms are required for a minimal model of the data. This model assumes that all radiative recombination has a sufficiently small activation energy that appears barrierless within the measurement window. The effect of this assumption is that the PL internal quantum efficiency (IQE) approaches unity at low temperatures. The best-fit model parameters are presented in Table I.

We find that $BaZrS_3$ and $CsPbBr_3$ feature a nonradiative recombination process with similar activation energy $E_a = 68 \pm 7$ and 86 ± 5 meV, respectively. This is apparent by eye in the Arrhenius plot [Fig. 2(a)], as both data sets have similar curvature and a knee at approximately the same temperature. However, the PL yield of $CsPbBr_3$ is over four orders of magnitude larger than that of $BaZrS_3$, and the data do not extrapolate toward the same yield in the low-temperature limit. The presence of nonradiative recombination mechanisms with similar activation energy belies the difference in PL intensity.

To explain the divergence in PL intensity, we invoke a second nonradiative recombination mechanism in $BaZrS_3$, with activation energy E_b too low to be determined in our measurement window. We also assume a similar second mechanism in $CsPbBr_3$ for consistency in the model function. By construction, the thermal scale E_b/k_B falls well below our experimental temperature window, and therefore, E_b cannot be determined by regression. This low-temperature process is saturated within the measured temperature range, and $e^{-E_b/k_BT} \approx 1$. With this assumption, we fix the temperature scale E_b/k_B at a low value and fit the data to determine B. In Fig. 2(b), we present a family of model functions with E_b varied manually; for E_b sufficiently small, its value has an insignificant impact on the fit results and our conclusions. The ratio B_{BZS}/B_{CPB} is meaningful, as it determines the measured difference in low-temperature PL yield between $BaZrS_3$ (BZS) and $CsPbBr_3$ (CPB). We find that

$$\frac{B_{BZS}}{B_{CPB}} = \frac{\left(k^0_{nr,b}/k_r\right)_{BZS}}{\left(k^0_{nr,b}/k_r\right)_{CPB}} = 28,181. \quad (3)$$

Both materials have comparable optical absorption coefficients near their band edge; therefore, we can approximate $(k_{r,CPB}/k_{r,BZS}) \approx \mathcal{O}(1)$. We therefore conclude that the rate

TABLE I. Best-fit parameters for PL yield, Eq. (2). Results are presented here for $E_b/k_B = 0$ K. In Table S2 of the SM [60], we present results for other choices of E_b/k_B.

Material	I_0 (photons/sec)	E_a (meV)	E_b/k_B (K)	A	B
$BaZrS_3$	6.7×10^{15}	68 ± 7	0	$(6.9 \pm 3.8) \times 10^{17}$	$(2.8 \pm 0.5) \times 10^{14}$
$CsPbBr_3$	4.3×10^{11}	86 ± 5	0	$(2.8 \pm 0.8) \times 10^{13}$	$(9.6 \pm 1.4) \times 10^{9}$

constant $k^0_{\mathrm{nr,b}}$ of low- (or zero-) barrier nonradiative recombination is $\mathcal{O}(10^4)$ times faster in $BaZrS_3$ than in $CsPbBr_3$.

We analyze the PL linewidth (Γ_{PL}) for insight into how excited states couple to lattice vibrations. In Fig. 2(b), we show the temperature dependence of Γ_{PL} of the main PL peak at the E_g for each material. We use multiple Gaussian peaks to fit the data, three for $CsPbBr_3$ and four for $BaZrS_3$. For both materials, the main PL peak is well modeled by two Gaussian peaks, and we determine Γ_{PL} numerically from the best-fit models. We fit Γ_{PL} to a relation describing thermal and nonthermal broadening, previously applied to halide perovskites [52]:

$$\Gamma_{\mathrm{PL}}(T) = \Gamma_0 + \frac{\gamma}{e^{E_{\mathrm{ph}}/k_{\mathrm{B}}T} - 1}, \tag{4}$$

where Γ_0 represents temperature-independent contributions to Γ_{PL}, such as heterogeneous broadening due to quenched structural disorder. The second term describes broadening due to coupling between excited states and lattice vibrations with characteristic energy E_{ph} and electron-phonon coupling constant γ. These lattice vibrations are likely longitudinal optical phonons (see below), and the electron-phonon interactions can be described through deformation potentials.

We find that luminescent band-edge states couple to vibrations with characteristic energy that is similar in both materials: $E_{\mathrm{ph}} = 24 \pm 7$ meV for $BaZrS_3$, and 17 ± 4 meV for $CsPbBr_3$ (see below). The electron-phonon coupling constant γ is larger for $BaZrS_3$ (200 ± 100 meV) than for $CsPbBr_3$ (50 ± 10 meV). γ is related to deformation potentials and polar optical coupling. The higher value in $BaZrS_3$ may be related to the stronger covalent nature of the Zr-S bonds compared to Pb-Br bonds: 32% covalent for Zr-S, compared to 26% for Pb-Br, according to the Pauling scale. This implies enhanced sensitivity of electron energies to bond angles in the chalcogenide, as we have studied previously [13,35]. We also see that $BaZrS_3$ has a larger heterogeneous broadening, Γ_0, than $CsPbBr_3$, reflecting a higher concentration of structural defects and other forms of nonthermal disorder. In addition to affecting the PL spectra, these factors affect how steeply optical absorption rises at the band gap, the width of the Urbach tail, and the phonon-limited charge transport mobility, and are therefore relevant to photovoltaic performance [65–67].

B. Raman scattering and phonon dynamics

The lower luminescence yield and larger PL broadening in $BaZrS_3$, compared to $CsPbBr_3$, are related to differences in lattice vibrations. To better understand these relationships, we turn to theoretical and experimental studies of the phonon spectra. In Fig. 3, we present the total (black) and partial (orange, green, and blue) vibrational density of states of $BaZrS_3$ (top) and $CsPbBr_3$ (bottom), calculated *ab initio* using the temperature-dependent effective potential (TDEP) method at 300 K (details in Sec. S2 of the SM [60,68–83]). The optical vibrations in $BaZrS_3$ span frequencies up to 430 cm^{-1} (53 meV), while those in $CsPbBr_3$ peak at 160 cm^{-1} (20 meV). This is due to the higher mass of the atoms in $CsPbBr_3$ and the more covalent character of the bonds in $BaZrS_3$ [84].

Longitudinal optical (LO) phonons couple to electronic excitations and likely contribute most to the temperature-dependent PL linewidth broadening. In Fig. 3, the vertical red lines provide a measure of the phonon LO character: As detailed in Sec. S2 of the SM [60], the LO character is estimated by computing the longitudinal charges for optical vibrations from the mode eigenvectors and the atomic Born charge tensors, projected on the [101] excitation direction, and divided by the vibration frequency to account for the average mode amplitudes. We see that $BaZrS_3$ has many phonons with prominent LO character along the [101] excitation direction, whereas $CsPbBr_3$ only shows one mode of appreciable LO character at $\approx$125 cm^{-1}. This factor likely contributes to the stronger temperature-dependent PL broadening in $BaZrS_3$ in addition to the higher deformation potentials.

The characteristic energy of lattice vibrations responsible for PL broadening in $CsPbBr_3$, $E_{\mathrm{ph}} \simeq 17$ meV ($\approx$140 cm^{-1}) is comparable to the most prominent LO phonon in the calculated spectrum. For $BaZrS_3$, $E_{\mathrm{ph}} \simeq 24$ meV ($\approx$190 cm^{-1}) falls roughly in the middle of the calculated spectrum. Likely, band-edge states couple to a diversity of lattice vibrations in both materials through polar optical coupling and deformation potentials, and the characteristic energy determined by PL broadening represents a distribution of processes. Similar conclusions have been reached in studies of ultrafast lattice rearrangement following optical excitation of halide perovskites, including $CsPbBr_3$ [85].

In Fig. 4, we present the low-frequency Raman spectra of $BaZrS_3$ and $CsPbBr_3$ measured in the temperature range 80–350 K. The spectra of $BaZrS_3$ and $CsPbBr_3$ are consistent with previous reports [58,86], and mode assignments can be found in Ref. [56,87]. In Sec. S3 of the SM [60], we present the Raman spectra of $BaZrS_3$ measured over a wider temperature range, from 10 to 875 K, showing no indication of a phase transition [14,88,89].

The Raman spectra of $CsPbBr_3$ exhibit sharp first-order peaks (one photon scattered by one vibration) [90] at low temperatures, which shift and broaden significantly with increasing temperature. These structural dynamics are characteristic of halide and certain oxide perovskites [53,91–93]. The broad, featureless spectra at high temperatures, combined with a rapid decrease in vibrational lifetime (evidenced by peak broadening), indicate the impact of anharmonic vibrational dynamics [23,52].

At low temperatures, the Raman spectra of $BaZrS_3$ resemble those of $CsPbBr_3$ and other halide perovskites [55,94], with a similar number of prominent peaks divided into doublets and triplets. The vibrations in $BaZrS_3$ are higher in frequency than those in $CsPbBr_3$. Unlike $CsPbBr_3$, the Raman peaks in $BaZrS_3$ remain sharp and distinct with increasing temperature, and even at 350 K, there is a scant signature of anharmonic dynamics. The harmonic dynamics in $BaZrS_3$ recall those in tetrahedrally bonded semiconductors (e.g., GaAs), in which vibrations along the stiff covalent bonds do not interact and change little with temperature [95,96].

We can more quantitatively compare the structural dynamics of $BaZrS_3$ and $CsPbBr_3$ by considering the temperature dependence of the phonon frequencies and linewidths. We model the Raman spectra as a convolution of pseudo-Voigt peaks multiplied by the Bose-Einstein occupation factor

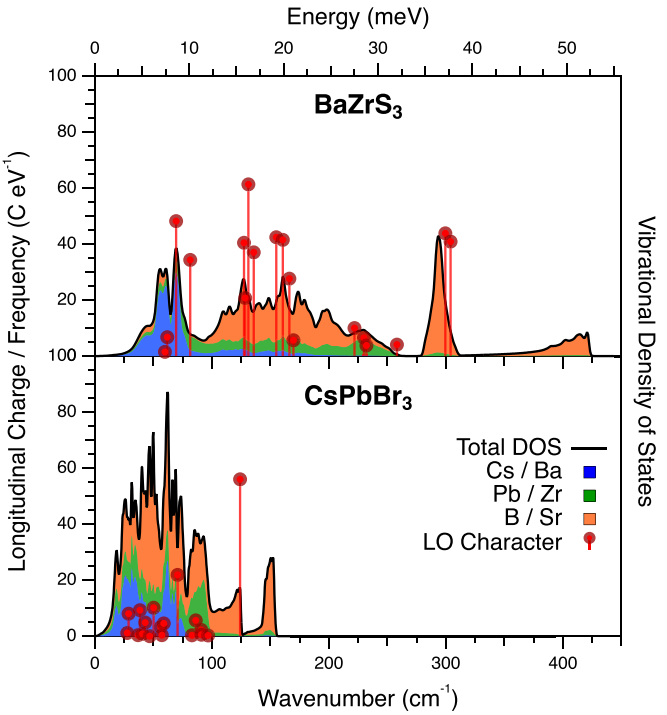

FIG. 3. Calculated room-temperature phonon density of states (DOS, right axis) of $BaZrS_3$ and $CsPbBr_3$. The colors indicate the partial contribution of the A (blue), M (green), and X (orange) ions in the AMX_3 formula. The red lines are the measure (left axis) of the LO character. The top and bottom axes label the abscissa in energy and wavenumber, respectively.

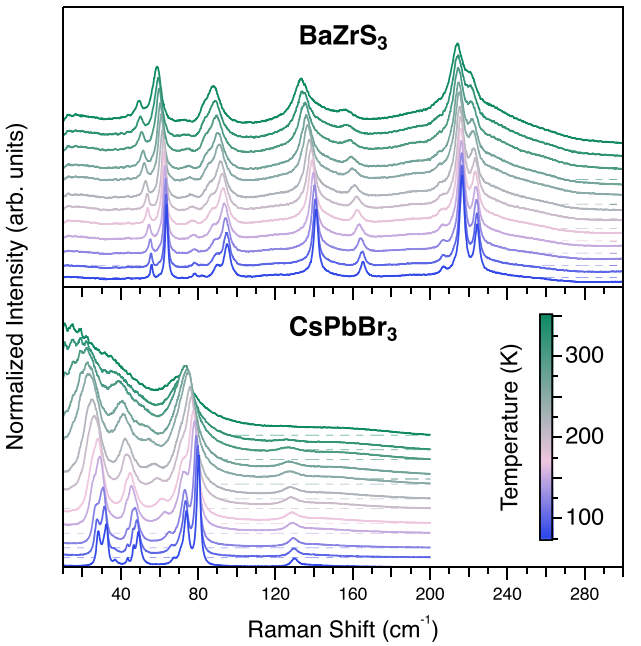

FIG. 4. Temperature-dependent Raman scattering spectra of $BaZrS_3$ and $CsPbBr_3$. Temperature is indicated by color. The individual data sets are shifted vertically for clarity; the dashed horizontal lines indicate the zero level for each data set.

[97–99] (see Sec. S3 of the SM [60]). We focus on the prominent peaks because they yield the most confident fits. In Fig. 5(a) we present the vibrational frequency (Ω) and linewidth (Γ_R) of the prominent first-order peaks of $BaZrS_3$ (left panel, orange) and $CsPbBr_3$ (right panel, purple). The frequency and linewidth data are divided by their values at 80 K for ease of comparison (for original values, see Sec. S3 of the SM [60]). The Raman peaks of $BaZrS_3$ red shift and broaden linearly with increasing temperature, as is expected from perturbation theory for weak anharmonic effects [100,101]. A slight change in slope near 200 K may relate to the observed increase in the low-frequency dielectric susceptibility in this same temperature range [12].

$CsPbBr_3$ exhibits a similar monotonic and linear trend in frequency and linewidth with increasing temperature up to 280 K, above which the data deviate substantially, including sharp blue shifts and rapidly increasing linewidth (see Fig. S8 of the SM [60]). We attribute these changes to two causes: (1) the thermal population of all the optical phonons above $T_{\text{Debye}} \approx 250$ K, and (2) the incipient orthorhombic-to-tetragonal phase transition at $T \approx 360$ K. Peak broadening with increasing temperature is attributed to the shortening of vibrational lifetime due to phonon-phonon scattering [98,100,101]. It is apparent that the structural dynamics of $BaZrS_3$ exhibit minor thermal effects and are less impacted by anharmonic vibrational interactions than the dynamics of $CsPbBr_3$ [100,101].

The extent of anharmonicity in the phonon dynamics can be further quantified by analyzing the deviation from linearity of the temperature dependence of the phonon frequencies and linewidths. A linear temperature dependence is expected within perturbation theory for weak phonon-phonon interactions. Therefore, strong and anharmonic interactions are indicated by deviations from linearity. In Fig. 5(b), we present the R^2 parameter and the absolute value of the slope ($|\alpha|$) of linear regression to the $\Omega(T)$ and $\Gamma_R(T)$ (for mean values, see Sec. S3 of the SM [60]). For $CsPbBr_3$, the R^2 values are far from unity, and the slopes are much larger than for $BaZrS_3$. This analysis further supports the conclusion that anharmonic effects in $BaZrS_3$ can be modeled as a weak perturbation, whereas in $CsPbBr_3$, they substantially change the lattice vibrational properties.

IV. DISCUSSION

Lead halide perovskites excel as PV absorbers largely due to their slow rates of defect-assisted Shockley-Read-Hall (SRH) nonradiative free energy loss. Electron-phonon interactions mediate SRH recombination processes, converting excited-state energy into phonons and heat [25,27,31,102]. Therefore, by focusing on vibrational properties and electron-phonon interactions, we can better understand the origin of the excellent PV performance of the halides and identify promising new semiconductors for thin-film PV.

Chalcogenide perovskites have an untested potential for PV mainly due to challenges in thin-film synthesis. There are few published measurements of the optoelectronic properties of chalcogenide perovskites, and the results are ambiguous. We reported time-resolved PL (TRPL) data that suggest long

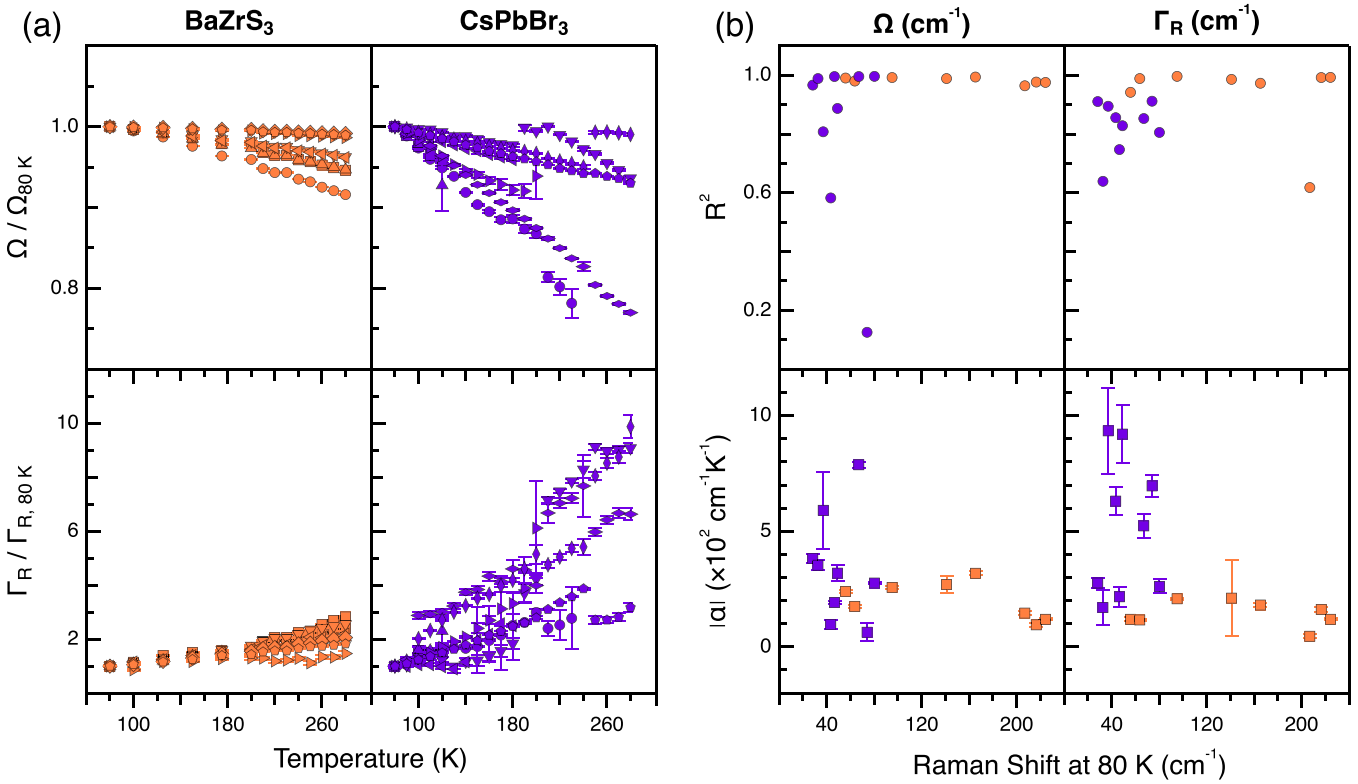

FIG. 5. Analysis of Raman Spectra: (a) Frequencies (Ω, top) and linewidths (Γ_R, bottom) of the first-order peaks of $BaZrS_3$ (left) and $CsPbBr_3$ (right) as a function of temperature, relative to the value at 80 K. Different markers mark different peaks. (b) Linear regression results (R^2, top, and slopes α, bottom) of the temperature-dependent frequencies (left) and linewidths (right) of $BaZrS_3$ and $CsPbBr_3$, between 80 and 280 K. The results are plotted as a function of peak frequency at 80 K. Orange and purple markers are for $BaZrS_3$ and $CsPbBr_3$, respectively. Error bars indicate one standard deviation as determined by the numerical fitting process.

radiative lifetimes in $BaZrS_3$ and the Ruddlesden-Popper compound $Ba_3Zr_2S_7$, comparable to lead halides and other high-performing PV materials such as CIGS [19]. Several research groups have reported band-edge PL measured from $BaZrS_3$ samples of various form factors, including solution-processed nanoparticles and thin films made by sulfurizing oxide precursors [16,18,20,21]. However, quantitative PL measurements (albeit on early-stage powder samples) suggest low quantum efficiency and low quasi-Fermi level splitting (i.e., open-circuit voltage potential) [9]. Our experience of measuring PL on $BaZrS_3$ single crystals is that many samples have weak or no measurable band-edge PL and that the band-edge PL can be strongly position dependent. To this point, the $BaZrS_3$ crystals used in our prior TRPL study were produced by the same process as the crystal studied here, but were prepared in different batches. We have observed similar variability in measuring PL on epitaxial thin films (unpublished). Substantial sample-to-sample variation, combined with challenges in synthesis and defect control, makes it difficult to assess the technological potential of chalcogenide perovskites.

We also note that the presence of long-lived traps in the detailed balance with only one band edge (e.g., electron traps with vanishing hole capture likelihood) would slow the decay to equilibrium after pulsed excitation. For a direct band-gap semiconductor such as $BaZrS_3$, this would be observed as a long TRPL lifetime, that could coexist with a low PL quantum yield.

SRH recombination is much faster in $BaZrS_3$ than in $CsPbBr_3$ due to an unidentified recombination pathway that is active even at low temperatures, implying that it has a very low thermal activation energy [Fig. 2(b)]. The theory of multi-phonon nonradiative recombination highlights the importance of the overlap between the vibrational wavefunctions of the initial and final electronic states, consistent with the Franck-Condon principle [50]. Model calculations for a harmonic lattice indicate a steep dependence of SRH recombination rate on phonon energy [102]. Lower phonon energy means more phonons are needed to participate in nonradiative recombination processes. Within this model, the overlap of vibrational wavefunctions is suppressed with increasing phonon number. Therefore, the lower phonon frequency in $CsPbBr_3$ compared to $BaZrS_3$ may explain the difference in SRH recombination rates, even if the concentration and properties of defects are similar.

The same harmonic model also predicts that SRH recombination rates increase with the extent of lattice distortion accompanying defect charge capture; this distortion can be parameterized by the Huang-Rhys factor [50,102]. These lattice distortions often result in long-lived charge trapping and are responsible for persistent photoconductivity in many semiconductors; it is related to DX-center phenomena in III-V compounds, and we termed it defect-level switching in the context of resistive switches [103–106]. There have been many studies of persistent photocon-

ductivity in halide perovskites. Still, there is no clear model for defects in $CsPbBr_3$ [107–110]. The timescale of photoconductivity decay in $BaZrS_3$ crystals depends on sample polishing, suggesting that defects introduced during plastic deformation (e.g., dislocations) may be effective charge traps with large Huang-Rhys factors [36]. However, these observations may not be directly relevant to the Huang-Rhys factors of recombination-active defects, which may differ from the traps that influence photoconductivity decay. Further, it has been suggested that polaronic effects resulting from strong charge-lattice coupling—including Fröhlich (i.e., large effective mass states) polarons and defect-localized polarons—may suppress SRH recombination rates by screening dissimilar charges [111,112]. It is likely that a full-quantum calculation of electron-phonon interactions, combined with first-principles modeling of the known crystal structures and the most likely recombination-active defects, will be required to resolve these questions over the role of strong electron-phonon coupling on SRH recombination rates.

The effect of anharmonic phonon-phonon interactions on SRH recombination remains an open question. It would be enlightening to compare a model calculation of vibrational wavefunction overlap during multiphonon recombination with and without anharmonic lattice vibrations and for varying Huang-Rhys factors for otherwise similar phonon energies. Model system calculations could help to understand the conflated effects of low-phonon energy, lattice distortion at defects, and anharmonic vibrations on SRH recombination rates. However, full-quantum calculations are likely needed to accurately model the differences in carrier capture rates between halide and chalcogenide perovskites.

The discussion to this point has focused on the effects of lattice vibrations on SRH recombination rates via the carrier capture processes. However, another significant unknown is the concentration of recombination-active defects. Anharmonic vibrations in halide perovskites indicate rather soft bonds, a pliable crystal lattice, and low-activation energy for ionic diffusion [113–115]. Therefore, anharmonic vibration in lead halide perovskites may improve optoelectronic performance by accelerating the elimination of point defects by annealing, even at room temperature (termed "self-healing") [51,116–119]. The same accelerated mass transport may hasten degradation mechanisms. $BaZrS_3$, in contrast, requires a high temperature to form and, therefore, is likely to retain quenched-in defects (e.g., chemical impurities). This suggests that the PL yield and PV performance of chalcogenide perovskites will depend more strongly on defect control during sample processing than the performance of halide perovskites.

Defect characterization by methods such as deep-level transient spectroscopy (DLTS) and related forms of impedance spectroscopy could directly measure defect concentrations and quantify the extent of self-healing [120–126]. Interpretation of DLTS data is challenging for halide perovskites due to mixed ionic-electronic conduction, but progress has been reported [127]. Similar studies have not yet been undertaken for chalcogenide perovskites.

V. CONCLUSIONS

We have presented a detailed spectroscopic comparison between two perovskite semiconductors, the chalcogenide $BaZrS_3$ and the well-studied halide $CsPbBr_3$. We find that the PL emission yield of $CsPbBr_3$ is over four orders of magnitude higher than that of $BaZrS_3$ for the single-crystal samples considered here, indicative of a far higher concentration of very low-barrier, nonradiative recombination centers in $BaZrS_3$. *Ab initio* simulations show that $BaZrS_3$ exhibits higher LO vibrational frequencies than $CsPbBr_3$: this may increase carrier capture cross sections due to Franck-Condon effects [50]. Raman scattering results suggest that the strongly anharmonic structural dynamics in $CsPbBr_3$, relative to $BaZrS_3$, may reduce defect concentration through accelerated solid-state diffusion and annealing [51].

We are optimistic that the fast SRH recombination rates observed here for $BaZrS_3$ can be reduced through sample processing. Large sample-to-sample variability, and preliminary results on $BaZrS_3$ epitaxial thin films (not shown), suggest that low PL yield may not be intrinsic to $BaZrS_3$. The usefulness of $BaZrS_3$ (and likely other chalcogenide perovskites) for optoelectronic applications will hinge on continued progress in defect control during synthesis and processing—as has been historically required for other semiconductors.

ACKNOWLEDGMENTS

We acknowledge the support of Dr. I. Pinkas (WIS) for help designing the experimental setup, Dr. L. Segev (WIS) for developing the Raman software, and Dr. S. Aharon (Princeton) for help in the synthesis of $CsPbBr_3$ crystals. O.Y. acknowledges funding from the European Research Council starting grant (850041 - ANHARMONIC). We acknowledge support from the MIT-Israel Zuckerman STEM Fund and the Sagol Weizmann-MIT Bridge Program. We acknowledge support from the United States-Israel Binational Science Foundation, Grant no. 2020270. We acknowledge support from the National Science Foundation (NSF) under Grant No. 1751736. We acknowledge support from the Skolkovo Institute of Science and Technology and the MIT-Skoltech Next Generation Program. K.Y. acknowledges support from the NSF Graduate Research Fellowship, Grant No. 1745302. B.Z. and J.R. acknowledge support from an ARO MURI with Award No. W911NF-21-1-0327, an NSF grant with Award No. DMR-2122071, and an ONR grant with Award No. N00014-23-1-2818. F.K. acknowledges support from the Swedish Research Council (VR) program 2020-04630, and the Swedish e-Science Research Centre (SeRC). The computations were enabled by resources provided by the National Academic Infrastructure for Supercomputing in Sweden (NAISS) at NSC and PDC partially funded by the Swedish Research Council through Grant Agreement No. 2022-06725.

[1] T. M. Brenner, D. A. Egger, L. Kronik, G. Hodes, and D. Cahen, Hybrid organic—inorganic perovskites: Low-cost semiconductors with intriguing charge-transport properties, Nat. Rev. Mater., 16011 (2016).

[2] M. Grätzel, The light and shade of perovskite solar cells, Nat. Mater. **13**, 838 (2014).

[3] S. D. Stranks and H. J. Snaith, Metal-halide perovskites for photovoltaic and light-emitting devices, Nat. Nanotechnol. **10**, 391 (2015).

[4] H. He, Q. Yu, H. Li, J. Li, J. Si, Y. Jin, N. Wang, J. Wang, J. He, X. Wang, Y. Zhang, and Z. Ye, Exciton localization in solution-processed organolead trihalide perovskites, Nat. Commun. **7**, 10896 (2016).

[5] D. Shi, V. Adinolfi, R. Comin, M. Yuan, E. Alarousu, A. Buin, Y. Chen, S. Hoogland, A. Rothenberger, K. Katsiev, Y. Losovyj, X. Zhang, P. A. Dowben, O. F. Mohammed, E. H. Sargent, and O. M. Bakr, Low trap-state density and long carrier diffusion in organolead trihalide perovskite single crystals, Science **347**, 519 (2015).

[6] S. D. Stranks, V. M. Burlakov, T. Leijtens, J. M. Ball, A. Goriely, and H. J. Snaith, Recombination kinetics in organic-inorganic perovskites: Excitons, free charge, and subgap states, Phys. Rev. Appl. **2**, 034007 (2014).

[7] Y. Yamada, T. Yamada, L. Q. Phuong, N. Maruyama, H. Nishimura, A. Wakamiya, Y. Murata, and Y. Kanemitsu, Dynamic optical properties of $CH_3NH_3PbI_3$ single crystals as revealed by one- and two-photon excited photoluminescence measurements, J. Am. Chem. Soc. **137**, 10456 (2015).

[8] C. Wehrenfennig, G. E. Eperon, M. B. Johnston, H. J. Snaith, and L. M. Herz, High charge carrier mobilities and lifetimes in organolead trihalide perovskites, Adv. Mater. **26**, 1584 (2014).

[9] S. Niu, H. Huyan, Y. Liu, M. Yeung, K. Ye, L. Blankemeier, T. Orvis, D. Sarkar, D. J. Singh, R. Kapadia, and J. Ravichandran, Bandgap control via structural and chemical tuning of transition metal perovskite chalcogenides, Adv. Mater. **29**, 1604733 (2017).

[10] R. Jaramillo and J. Ravichandran, In praise and in search of highly-polarizable semiconductors: Technological promise and discovery strategies, APL Mater. **7**, 100902 (2019).

[11] Y.-Y. Sun, M. L. Agiorgousis, P. Zhang, and S. Zhang, Chalcogenide perovskites for photovoltaics, Nano Lett. **15**, 581 (2015).

[12] S. Filippone, B. Zhao, S. Niu, N. Z. Koocher, D. Silevitch, I. Fina, J. M. Rondinelli, J. Ravichandran, and R. Jaramillo, Discovery of highly polarizable semiconductors $BaZrS_3$ and $Ba_3Zr_2S_7$, Phys. Rev. Mater. **4**, 091601(R) (2020).

[13] K. Ye, N. Z. Koocher, S. Filippone, S. Niu, B. Zhao, M. Yeung, S. Bone, A. J. Robinson, P. Vora, A. Schleife, L. Ju, A. Boubnov, J. M. Rondinelli, J. Ravichandran, and R. Jaramillo, Low-energy electronic structure of perovskite and Ruddlesden-Popper semiconductors in the Ba-Zr-S system probed by bond-selective polarized x-ray absorption spectroscopy, infrared reflectivity, and Raman scattering, Phys. Rev. B **105**, 195203 (2022).

[14] S. Niu, J. Milam-Guerrero, Y. Zhou, K. Ye, B. Zhao, B. C. Melot, and J. Ravichandran, Thermal stability study of transition metal perovskite sulfides, J. Mater. Res. **33**, 4135 (2018).

[15] I. Sadeghi, K. Ye, M. Xu, Y. Li, J. M. LeBeau, and R. Jaramillo, Making $BaZrS_3$ chalcogenide perovskite thin films by molecular beam epitaxy, Adv. Funct. Mater. **31**, 2105563 (2021).

[16] X. Wei, H. Hui, C. Zhao, C. Deng, M. Han, Z. Yu, A. Sheng, P. Roy, A. Chen, J. Lin, D. F. Watson, Y.-Y. Sun, T. Thomay, S. Yang, Q. Jia, S. Zhang, and H. Zeng, Realization of $BaZrS_3$ chalcogenide perovskite thin films for optoelectronics, Nano Energy **68**, 104317 (2020).

[17] M. Surendran, H. Chen, B. Zhao, A. S. Thind, S. Singh, T. Orvis, H. Zhao, J.-K. Han, H. Htoon, M. Kawasaki, R. Mishra, and J. Ravichandran, Epitaxial thin films of a chalcogenide perovskite, Chem. Mater. **33**, 7457 (2021).

[18] C. Comparotto, A. Davydova, T. Ericson, L. Riekehr, M. V. Moro, T. Kubart, and J. Scragg, Chalcogenide perovskite $BaZrS_3$: Thin film growth by sputtering and rapid thermal processing, ACS Appl. Energy Mater. **3**, 2762 (2020).

[19] K. Ye, B. Zhao, B. T. Diroll, J. Ravichandran, and R. Jaramillo, Time-resolved photoluminescence studies of perovskite chalcogenides, Faraday Discuss. **239**, 146 (2022).

[20] A. Pradhan, M. Uible, S. Agarwal, J. Turnley, S. Khandelwal, J. Peterson, D. Blach, R. Swope, L. Huang, S. Bart, and R. Agrawal, Synthesis of $BaZrS_3$ and $BaHfS_3$ chalcogenide perovskite films using single-phase molecular precursors at moderate temperatures, Angew. Chem., Int. Ed. **62**, e202301049 (2023).

[21] R. Yang, A. D. Jess, C. Fai, and C. J. Hages, Low-temperature, solution-based synthesis of luminescent chalcogenide perovskite $BaZrS_3$ nanoparticles, J. Am. Chem. Soc. **144**, 15928 (2022).

[22] R. Sharma, Z. Dai, L. Gao, T. M. Brenner, L. Yadgarov, J. Zhang, Y. Rakita, R. Korobko, A. M. Rappe, and O. Yaffe, Elucidating the atomistic origin of anharmonicity in tetragonal $CH_3NH_3PbI_3$ with Raman scattering, Phys. Rev. Mater. **4**, 092401(R) (2020).

[23] O. Yaffe, Y. Guo, L. Z. Tan, D. A. Egger, T. D. Hull, C. C. Stoumpos, F. Zheng, T. F. Heinz, L. Kronik, M. G. Kanatzidis, J. S. Owen, A. M. Rappe, M. A. Pimenta, and L. E. Brus, Local polar fluctuations in lead halide perovskite crystals, Phys. Rev. Lett. **118**, 136001 (2017).

[24] Y. Guo, O. Yaffe, D. W. Paley, A. N. Beecher, T. D. Hull, G. Szpak, J. S. Owen, L. E. Brus, and M. A. Pimenta, Interplay between organic cations and inorganic framework and incommensurability in hybrid lead-halide perovskite $CH_3NH_3PbBr_3$, Phys. Rev. Mater. **1**, 042401(R) (2017).

[25] M. Mayers, L. Z. Tan, D. A. Egger, A. M. Rappe, and D. R. Reichman, How lattice and charge fluctuations control carrier dynamics in halide perovskites, Nano Lett. **18**, 8041 (2018).

[26] L. D. Whalley, J. M. Skelton, J. M. Frost, and A. Walsh, Phonon anharmonicity, lifetimes, and thermal transport in $CH_3NH_3PbI_3$ from many-body perturbation theory, Phys. Rev. B **94**, 220301(R) (2016).

[27] D. A. Egger, A. Bera, D. Cahen, G. Hodes, T. Kirchartz, L. Kronik, R. Lovrincic, A. M. Rappe, D. R. Reichman, and O. Yaffe, What remains unexplained about the properties of halide perovskites? Adv. Mater. **30**, 1800691 (2018).

[28] F. Panzer, C. Li, T. Meier, A. Köhler, and S. Huettner, Impact of structural dynamics on the optical properties of methylammonium lead iodide perovskites, Adv. Energy Mater. **7**, 1700286 (2017).

[29] S. A. Seidl, X. Zhu, G. Reuveni, S. Aharon, C. Gehrmann, S. Caicedo-Dávila, O. Yaffe, and D. A. Egger, Anharmonic

fluctuations govern the band gap of halide perovskites, Phys. Rev. Mater. **7**, L092401 (2023).

[30] C. Gehrmann and D. A. Egger, Dynamic shortening of disorder potentials in anharmonic halide perovskites, Nat. Commun. **10**, 3141 (2019).

[31] M. J. Schilcher, P. J. Robinson, D. J. Abramovitch, L. Z. Tan, A. M. Rappe, D. R. Reichman, and D. A. Egger, The significance of polarons and dynamic disorder in halide perovskites, ACS Energy Lett. **6**, 2162 (2021).

[32] S. Niu, B. Zhao, K. Ye, E. Bianco, J. Zhou, M. E. McConney, C. Settens, R. Haiges, R. Jaramillo, and J. Ravichandran, Crystal growth and structural analysis of perovskite chalcogenide $BaZrS_3$ and Ruddlesden-Popper phase $Ba_3Zr_2S_7$, J. Mater. Res. **34**, 3819 (2019).

[33] T. Lanigan-Atkins, X. He, M. J. Krogstad, D. M. Pajerowski, D. L. Abernathy, G. N. Xu, Z. Xu, D. Y. Chung, M. G. Kanatzidis, S. Rosenkranz, R. Osborn, and O. Delaire, Two-dimensional overdamped fluctuations of the soft perovskite lattice in $CsPbBr_3$, Nat. Mater. **20**, 977 (2021).

[34] Y. Nishigaki, T. Nagai, M. Nishiwaki, T. Aizawa, M. Kozawa, K. Hanzawa, Y. Kato, H. Sai, H. Hiramatsu, H. Hosono, and H. Fujiwara, Extraordinary strong band-edge absorption in distorted chalcogenide perovskites, Solar RRL **4**, 1900555 (2020).

[35] W. Li, S. Niu, B. Zhao, R. Haiges, Z. Zhang, J. Ravichandran, and A. Janotti, Band gap evolution in Ruddlesden-Popper phases, Phys. Rev. Mater. **3**, 101601(R) (2019).

[36] B. Zhao, H. Chen, R. Ahsan, F. Hou, E. R. Hoglund, S. Singh, M. Shanmugasundaram, H. Zhao, A. V. Krayev, H. Htoon, P. E. Hopkins, J. Seidel, R. Kapadia, and J. Ravichandran, Photoconductive effects in single crystals of $BaZrS_3$, ACS Photonics **11**, 1109 (2024).

[37] I. Sadeghi, J. Van Sambeek, T. Simonian, M. Xu, K. Ye, T. Cai, V. Nicolosi, J. M. LeBeau, and R. Jaramillo, Expanding the perovskite periodic table to include chalcogenide alloys with tunable band gap spanning 1.5–1.9 eV, Adv. Funct. Mater. **33**, 2304575 (2023).

[38] K. Ye, I. Sadeghi, M. Xu, J. Van Sambeek, T. Cai, J. Dong, R. Kothari, J. LeBeau, and R. Jaramillo, A Processing route to chalcogenide perovskites alloys with tunable band gap via anion exchange, Adv. Func. Mater. 2405135 (2024).

[39] N. Kumar, J. Rani, and R. Kurchania, Advancement in $CsPbBr_3$ inorganic perovskite solar cells: Fabrication, efficiency and stability, Solar Energy **221**, 197 (2021).

[40] S. Ullah, J. Wang, P. Yang, L. Liu, S.-E. Yang, T. Xia, H. Guo, and Y. Chen, All-inorganic $CsPbBr_3$ perovskite: A promising choice for photovoltaics, Mater. Adv. **2**, 646 (2021).

[41] L. Clinckemalie, D. Valli, M. B. Roeffaers, J. Hofkens, B. Pradhan, and E. Debroye, Challenges and opportunities for $CsPbBr_3$ perovskites in low- a nd high-energy radiation detection, ACS Energy Lett. **6**, 1290 (2021).

[42] J. Yu, G. Liu, C. Chen, Y. Li, M. Xu, T. Wang, G. Zhao, and L. Zhang, Perovskite $CsPbBr_3$ crystals: Growth and applications, J. Mater. Chem. C **8**, 6326 (2020).

[43] P. Cheng, Z. Liu, R. Kang, J. Zhou, X. Wang, J. Zhao, and Z. Zuo, Growth and high-performance photodetectors of $CsPbBr_3$ single crystals, ACS Omega **8**, 26351 (2023).

[44] Y. Rakita, N. Kedem, S. Gupta, A. Sadhanala, V. Kalchenko, M. L. Böhm, M. Kulbak, R. H. Friend, D. Cahen, and G. Hodes, Low-temperature solution-grown $CsPbBr_3$ single crystals and their characterization, Cryst. Growth Des. **16**, 5717 (2016).

[45] Y. He, L. Matei, H. J. Jung, K. M. McCall, M. Chen, C. C. Stoumpos, Z. Liu, J. A. Peters, D. Y. Chung, B. W. Wessels, M. R. Wasielewski, V. P. Dravid, A. Burger, and M. G. Kanatzidis, High spectral resolution of gamma-rays at room temperature by perovskite $CsPbBr_3$ single crystals, Nat. Commun. **9**, 1609 (2018).

[46] M. Zhang, Z. Zheng, Q. Fu, Z. Chen, J. He, S. Zhang, L. Yan, Y. Hu, and W. Luo, Growth and characterization of all-inorganic lead halide perovskite semiconductor $CsPbBr_3$ single crystals, CrystEngComm **19**, 6797 (2017).

[47] J. Cheng, Z. Fan, and J. Dong, Research progress of green solvent in $CsPbBr_3$ perovskite solar cells, Nanomaterials **13**, 991 (2023).

[48] Y. Feng, L. Pan, H. Wei, Y. Liu, Z. Ni, J. Zhao, P. N. Rudd, L. R. Cao, and J. Huang, Low defects density $CsPbBr_3$ single crystals grown by an additive assisted method for gamma-ray detection, J. Mater. Chem. C **8**, 11360 (2020).

[49] D. N. Dirin, I. Cherniukh, S. Yakunin, Y. Shynkarenko, and M. V. Kovalenko, Solution-grown $CsPbBr_3$ perovskite single crystals for photon detection, Chem. Mater. **28**, 8470 (2016).

[50] B. Das, I. Aguilera, U. Rau, and T. Kirchartz, What is a deep defect? Combining Shockley-Read-Hall statistics with multiphonon recombination theory, Phys. Rev. Mater. **4**, 024602 (2020).

[51] D. Cahen, L. Kronik, and G. Hodes, Are defects in lead-halide perovskites healed, tolerated, or both? ACS Energy Lett. **6**, 4108 (2021).

[52] Y. Guo, O. Yaffe, T. D. Hull, J. S. Owen, D. R. Reichman, and L. E. Brus, Dynamic emission stokes shift and liquid-like dielectric solvation of band edge carriers in lead-halide perovskites, Nat. Commun. **10**, 1175 (2019).

[53] M. Menahem, N. Benshalom, M. Asher, S. Aharon, R. Korobko, O. Hellman, and O. Yaffe, Disorder origin of Raman scattering in perovskite single crystals, Phys. Rev. Mater. **7**, 044602 (2023).

[54] D. Han, K. Yang, C. Bai, F. Chen, Z. Sun, Y. Wang, H. Ji, Z. Yang, and X. Tang, Thermal and chemical durability of metal halide perovskite $CsPbBr_3$ single crystals, Chem. Eng. J. **475**, 146209 (2023).

[55] M. Menahem, Z. Dai, S. Aharon, R. Sharma, M. Asher, Y. Diskin-Posner, R. Korobko, A. M. Rappe, and O. Yaffe, Strongly anharmonic octahedral tilting in two-dimensional hybrid halide perovskites, ACS Nano **15**, 10153 (2021).

[56] R. Sharma, M. Menahem, Z. Dai, L. Gao, T. M. Brenner, L. Yadgarov, J. Zhang, Y. Rakita, R. Korobko, I. Pinkas, A. M. Rappe, and O. Yaffe, Lattice mode symmetry analysis of the orthorhombic phase of methylammonium lead iodide using polarized Raman, Phys. Rev. Mater. **4**, 051601(R) (2020).

[57] M. Asher, D. Angerer, R. Korobko, Y. Diskin-Posner, D. A. Egger, and O. Yaffe, Anharmonic lattice vibrations in small-molecule organic semiconductors, Adv. Mater. **32**, 1908028 (2020).

[58] A. Cohen, T. M. Brenner, J. Klarbring, R. Sharma, D. H. Fabini, R. Korobko, P. K. Nayak, O. Hellman, and O. Yaffe, Diverging expressions of anharmonicity in halide perovskites, Adv. Mater. **34**, 2107932 (2022).

[59] M. Asher, M. Bardini, L. Catalano, R. Jouclas, G. Schweicher, J. Liu, R. Korobko, A. Cohen, Y. Geerts, D. Beljonne, and O. Yaffe, Mechanistic view on the order-disorder phase transition in amphidynamic crystals, J. Phys. Chem. Lett. **14**, 1570 (2023).

[60] See Supplemental Material at http://link.aps.org/supplemental/10.1103/PhysRevMaterials.8.085402 for additional Raman spectra and fitting, derivations of the equations for the numerical simulation and additional results, and fit results to the model.

[61] J. W. Bennett, I. Grinberg, and A. M. Rappe, Effect of substituting of S for O: The sulfide perovskite BaZrS 3 investigated with density functional theory, Phys. Rev. B **79**, 235115 (2009).

[62] G. Ermolaev, A. P. Pushkarev, A. Zhizhchenko, A. A. Kuchmizhak, I. Iorsh, I. Kruglov, A. Mazitov, A. Ishteev, K. Konstantinova, D. Saranin, A. Slavich, D. Stosic, E. S. Zhukova, G. Tselikov, A. Di Carlo, A. Arsenin, K. S. Novoselov, S. V. Makarov, and V. S. Volkov, Giant and tunable excitonic optical anisotropy in single-crystal halide perovskites, Nano Lett. **23**, 2570 (2023).

[63] D. Bimberg, M. Sondergeld, and E. Grobe, Thermal dissociation of excitons bounds to neutral acceptors in high-purity GaAs, Phys. Rev. B **4**, 3451 (1971).

[64] J. D. Lambkin, L. Considine, S. Walsh, G. M. O'Connor, C. J. McDonagh, and T. J. Glynn, Temperature dependence of the photoluminescence intensity of ordered and disordered $In_{0.48}Ga_{0.52}P$, Appl. Phys. Lett. **65**, 73 (1994).

[65] M. H. Wolter, R. Carron, E. Avancini, B. Bissig, T. P. Weiss, S. Nishiwaki, T. Feurer, S. Buecheler, P. Jackson, W. Witte, and S. Siebentritt, How band tail recombination influences the open-circuit voltage of solar cells, Prog. Photovoltaics: Res. Appl. **30**, 702 (2022).

[66] X. Wang, D. Yu, and S. Xu, Determination of absorption coefficients and Urbach tail depth of ZnO below the bandgap with two-photon photoluminescence, Opt. Express **28**, 13817 (2020).

[67] N. Falsini, G. Roini, A. Ristori, N. Calisi, F. Biccari, and A. Vinattieri, Analysis of the Urbach tail in cesium lead halide perovskites, J. Appl. Phys. **131**, 010902 (2022).

[68] F. Knoop, N. Shulumba, A. Castellano, J. P. A. Batista, R. Farris, M. J. Verstraete, M. Heine, D. Broido, D. S. Kim, J. Klarbring, I. A. Abrikosov, S. I. Simak, and O. Hellman, TDEP: Temperature dependent effective potentials, J. Open Source Software **9**, 6150 (2024).

[69] N. Benshalom, G. Reuveni, R. Korobko, O. Yaffe, and O. Hellman, Dielectric response of rock-salt crystals at finite temperatures from first principles, Phys. Rev. Mater. **6**, 033607 (2022).

[70] A. v. Roekeghem, J. Carrete, and N. Mingo, Quantum self-consistent ab-initio lattice dynamics, Comput. Phys. Commun. **263**, 107945 (2021).

[71] P. Giannozzi, O. Baseggio, P. Bonfà, D. Brunato, R. Car, I. Carnimeo, C. Cavazzoni, S. d. Gironcoli, P. Delugas, F. F. Ruffino, A. Ferretti, N. Marzari, I. Timrov, A. Urru, and S. Baroni, Quantum ESPRESSO toward the exascale, J. Chem. Phys. **152**, 154105 (2020).

[72] R. Bianco, I. Errea, L. Paulatto, M. Calandra, and F. Mauri, Second-order structural phase transitions, free energy curvature, and temperature-dependent anharmonic phonons in the self-consistent harmonic approximation: Theory and stochastic implementation, Phys. Rev. B **96**, 014111 (2017).

[73] N. Shulumba, O. Hellman, and A. J. Minnich, Intrinsic localized mode and low thermal conductivity of PbSe, Phys. Rev. B **95**, 014302 (2017).

[74] P. Giannozzi, O. Andreussi, T. Brumme, O. Bunau, M. B. Nardelli, M. Calandra, R. Car, C. Cavazzoni, D. Ceresoli, M. Cococcioni, N. Colonna, I. Carnimeo, A. D. Corso, S. de Gironcoli, P. Delugas, R. A. DiStasio, Jr, A. Ferretti, A. Floris, G. Fratesi, G. Fugallo *et al.*, Advanced capabilities for materials modelling with Quantum ESPRESSO, J. Phys.: Condens. Matter **29**, 465901 (2017).

[75] M. Schlipf and F. Gygi, Optimization algorithm for the generation of ONCV pseudopotentials, Comput. Phys. Commun. **196**, 36 (2015).

[76] O. Hellman and I. A. Abrikosov, Temperature-dependent effective third-order interatomic force constants from first principles, Phys. Rev. B **88**, 144301 (2013).

[77] D. R. Hamann, Optimized norm-conserving Vanderbilt pseudopotentials, Phys. Rev. B **88**, 085117 (2013).

[78] A. Jain, S. P. Ong, G. Hautier, W. Chen, W. D. Richards, S. Dacek, S. Cholia, D. Gunter, D. Skinner, G. Ceder, and K. A. Persson, Commentary: The materials project: A materials genome approach to accelerating materials innovation, APL Mater. **1**, 011002 (2013).

[79] P. Giannozzi, S. Baroni, N. Bonini, M. Calandra, R. Car, C. Cavazzoni, D. Ceresoli, G. L. Chiarotti, M. Cococcioni, I. Dabo, A. D. Corso, S. d. Gironcoli, S. Fabris, G. Fratesi, R. Gebauer, U. Gerstmann, C. Gougoussis, A. Kokalj, M. Lazzeri, L. Martin-Samos *et al.*, QUANTUM ESPRESSO: A modular and open-source software project for quantum simulations of materials, J. Phys.: Condens. Matter **21**, 395502 (2009).

[80] V. Blum, R. Gehrke, F. Hanke, P. Havu, V. Havu, X. Ren, K. Reuter, and M. Scheffler, *Ab initio* molecular simulations with numeric atom-centered orbitals, Comput. Phys. Commun. **180**, 2175 (2009).

[81] A. E. Mattsson, R. Armiento, J. Paier, G. Kresse, J. M. Wills, and T. R. Mattsson, The AM05 density functional applied to solids, J. Chem. Phys. **128**, 084714 (2008).

[82] R. Armiento and A. E. Mattsson, Functional designed to include surface effects in self-consistent density functional theory, Phys. Rev. B **72**, 085108 (2005).

[83] J. P. Perdew, K. Burke, and M. Ernzerhof, Generalized gradient approximation made simple, Phys. Rev. Lett. **77**, 3865 (1996).

[84] M. Fox, Phonons, in *Optical Properties of Solids*, 2nd ed. (Oxford University Press, New York, 2010), pp. 273–276.

[85] N. Yazdani, M. I. Bodnarchuk, F. Bertolotti, N. Masciocchi, I. Fureraj, B. Guzelturk, B. L. Cotts, M. Zajac, G. Rainò, M. Jansen, S. C. Boehme, M. Yarema, M. F. Lin, M. Kozina, A. Reid, X. Shen, S. Weathersby, X. Wang, E. Vauthey, A. Guagliardi *et al.*, Coupling to octahedral tilts in halide perovskite nanocrystals induces phonon-mediated attractive interactions between excitons, Nat. Phys. **20**, 47 (2024).

[86] S. Perera, H. Hui, C. Zhao, H. Xue, F. Sun, C. Deng, N. Gross, C. Milleville, X. Xu, D. F. Watson, B. Weinstein, Y.-Y. Sun, S. Zhang, and H. Zeng, Chalcogenide perovskites–an emerging class of ionic semiconductors, Nano Energy **22**, 129 (2016).

[87] N. Gross, Y.-Y. Sun, S. Perera, H. Hui, X. Wei, S. Zhang, H. Zeng, and B. A. Weinstein, Stability and band-gap tuning of the chalcogenide perovskite $BaZrS_3$ in Raman and optical investigations at high pressures, Phys. Rev. Appl. **8**, 044014 (2017).

[88] J. Xu, Y. Fan, W. Tian, L. Ye, Y. Zhang, Y. Tian, Y. Han, and Z. Shi, Enhancing the optical absorption of chalcogenide perovskite $BaZrS_3$ by optimizing the synthesis and post-processing conditions, J. Solid State Chem. **307**, 122872 (2022).

[89] Z. Yu, X. Wei, Y. Zheng, H. Hui, M. Bian, S. Dhole, J.-H. Seo, Y.-Y. Sun, Q. Jia, S. Zhang, S. Yang, and H. Zeng, Chalcogenide perovskite $BaZrS_3$ thin-film electronic and optoelectronic devices by low temperature processing, Nano Energy **85**, 105959 (2021).

[90] M. Cardona and G. Guntherodt, *Light Scattering in Solids II - Basic Concepts and Instrumentation* (Springer-Verlag, Berlin, 1982), pp. 1–252.

[91] C. H. Perry, J. H. Fertel, and T. F. McNelly, Temperature dependence of the Raman spectrum of $SrTiO_3$ and $KTaO_3$, J. Chem. Phys. **47**, 1619 (1967).

[92] P. McMillan and N. Ross, The Raman spectra of several orthorhombic calcium oxide perovskites, Phys. Chem. Miner. **16**, 21 (1988).

[93] R. Ouillon, J.-P. Pinan-Lucarre, P. Ranson, P. Pruzan, S. K. Mishra, R. Ranjan, and D. Pandey, A Raman scattering study of the phase transitions in $SrTiO_3$ and in the mixed system $(Sr_{1-x}Ca_x)TiO_3$ at ambient pressure from T = 300 K down to 8 K, J. Phys.: Condens. Matter **14**, 2079 (2002).

[94] G. Reuveni, Y. Diskin-Posner, C. Gehrmann, S. Godse, G. G. Gkikas, I. Buchine, S. Aharon, R. Korobko, C. C. Stoumpos, D. A. Egger, and O. Yaffe, Static and dynamic disorder in formamidinium lead bromide single crystals, J. Phys. Chem. Lett. **14**, 1288 (2023).

[95] M. Born and M. Bradburn, The theory of the Raman effect in crystals, in particular rocksalt, Proc. R. Soc. A **188**, 161 (1947).

[96] P. Y. Yu and M. Cardona, *Fundamentals of Semiconductors, Physics and Materials Properties*, 4th ed. (Springer, Berlin/Heidelberg, 2010) p. 775.

[97] P. C. Kwok, Green's function method in lattice dynamics, in *Green's Function Method in Lattice Dynamics*, Solid State Physics, edited by F. Seitz, D. Turnbull, and H. Ehrenreich (Academic Press, New York, 1968), Vol. 20, pp. 213–303.

[98] A. A. Maradudin, E. W. Montroll, G. H. Weiss, and I. P. Ipatova, *Theory of Lattice Dynamics in the Harmonic Approximation* (Academic Press, New York, 1971), pp. 1–67, 2nd ed.

[99] S. A. Safran, G. Dresselhaus, and B. Lax, Theory of spin-disorder Raman scattering in magnetic semiconductors, Phys. Rev. B **16**, 2749 (1977).

[100] E. Haro, M. Balkanski, R. F. Wallis, and K. H. Wanser, Theory of the anharmonic damping and shift of the Raman mode in silicon, Phys. Rev. B **34**, 5358 (1986).

[101] J. Menéndez and M. Cardona, Temperature dependence of the first-order Raman scattering by phonons in Si, Ge, and α–Sn : Anharmonic effects, Phys. Rev. B **29**, 2051 (1984).

[102] T. Kirchartz, T. Markvart, U. Rau, and D. A. Egger, Impact of small phonon energies on the charge-carrier lifetimes in metal-halide perovskites, J. Phys. Chem. Lett. **9**, 939 (2018).

[103] D. V. Lang and R. A. Logan, Large-lattice-relaxation model for persistent photoconductivity in compound semiconductors, Phys. Rev. Lett. **39**, 635 (1977).

[104] P. M. Mooney, Deep donor levels (DX centers) in III-V semiconductors, J. Appl. Phys. **67**, R1 (1990).

[105] H. Yin, A. Akey, and R. Jaramillo, Large and persistent photoconductivity due to hole-hole correlation in CdS, Phys. Rev. Mater. **2**, 084602 (2018).

[106] H. Yin, A. Kumar, J. M. LeBeau, and R. Jaramillo, Defect-level switching for highly nonlinear and hysteretic electronic devices, Phys. Rev. Appl. **15**, 014014 (2021).

[107] Z. Liu, J. A. Peters, K. S. Bayikadi, V. Klepov, L. Pan, I. R. Pandey, M. G. Kanatzidis, and B. W. Wessels, Defects of perovskite semiconductor $CsPbBr_3$ investigated via photoluminescence and thermally stimulated current spectroscopies, J. Appl. Phys. **134**, 245101 (2023).

[108] A. V. Cohen, D. A. Egger, A. M. Rappe, and L. Kronik, Breakdown of the static picture of defect energetics in halide perovskites: The case of the br vacancy in $CsPbBr_3$, J. Phys. Chem. Lett. **10**, 4490 (2019).

[109] J. Kang and L. W. Wang, High defect tolerance in lead halide perovskite $CsPbBr_3$, J. Phys. Chem. Lett. **8**, 489 (2017).

[110] M. Sebastian, J. A. Peters, C. C. Stoumpos, J. Im, S. S. Kostina, Z. Liu, M. G. Kanatzidis, A. J. Freeman, and B. W. Wessels, Excitonic emissions and above-band-gap luminescence in the single-crystal perovskite semiconductors $CsPbBr_3$ and $CsPbCl_3$, Phys. Rev. B **92**, 235210 (2015).

[111] D. Emin, Barrier to recombination of oppositely charged large polarons, J. Appl. Phys. **123**, 055105 (2018).

[112] C. Franchini, M. Reticcioli, M. Setvin, and U. Diebold, Polarons in materials, Nat. Rev. Mater. **6**, 560 (2021).

[113] T. M. Brenner, C. Gehrmann, R. Korobko, T. Livneh, D. A. Egger, and O. Yaffe, Anharmonic host-lattice dynamics enable fast ion conduction in superionic AgI, Phys. Rev. Mater. **4**, 115402 (2020).

[114] D. T. Limmer and N. S. Ginsberg, Photoinduced phase separation in the lead halides is a polaronic effect, J. Chem. Phys. **152**, 230901 (2020).

[115] Y.-C. Zhao, W.-K. Zhou, X. Zhou, K.-H. Liu, D.-P. Yu, and Q. Zhao, Quantification of light-enhanced ionic transport in lead iodide perovskite thin films and its solar cell applications, Sci. Appl. **6**, e16243 (2017).

[116] S. Aharon, D. R. Ceratti, N. P. Jasti, L. Cremonesi, Y. Feldman, M. A. C. Potenza, G. Hodes, and D. Cahen, 2D Pb-halide perovskites can self-heal photodamage better than 3d ones, Adv. Funct. Mater. **32**, 2113354 (2022).

[117] B. P. Finkenauer, Akriti, K. Ma, and L. Dou, Degradation and self-healing in perovskite solar cells, ACS Appl. Mater. Interfaces **14**, 24073 (2022).

[118] D. R. Ceratti, Y. Rakita, L. Cremonesi, R. Tenne, V. Kalchenko, M. Elbaum, D. Oron, M. A. C. Potenza, G. Hodes, and D. Cahen, Self-healing inside $APbBr_3$ halide perovskite crystals, Adv. Mater. **30**, 1706273 (2018).

[119] S. Parida, S. Kumar, S. Cherf, S. Aharon, D. Cahen, and B. Eren, Self-healing and -repair of nanomechanical damages in lead halide perovskites, Adv. Funct. Mater. **33**, 2304278 (2023).

[120] E. M. Hutter, G. E. Eperon, S. D. Stranks, and T. J. Savenije, Charge carriers in planar and meso-structured

organic–inorganic perovskites: Mobilities, lifetimes, and concentrations of trap states, J. Phys. Chem. Lett. **6**, 3082 (2015).

[121] Y. Bi, E. M. Hutter, Y. Fang, Q. Dong, J. Huang, and T. J. Savenije, Charge carrier lifetimes exceeding 15 μs in methylammonium lead iodide single crystals, J. Phys. Chem. Lett **7**, 923 (2016).

[122] G. Xing, N. Mathews, S. S. Lim, N. Yantara, X. Liu, D. Sabba, M. Grätzel, S. Mhaisalkar, and T. C. Sum, Low-temperature solution-processed wavelength-tunable perovskites for lasing, Nat. Mater. **13**, 476 (2014).

[123] Y. Lei, Y. Xu, M. Wang, G. Zhu, Z. Jin, Y. Lei, Y. Xu, M. Wang, Z. Jin, and G. Zhu, Origin, influence, and countermeasures of defects in perovskite solar cells, Small **17**, 2005495 (2021).

[124] V. M. Le Corre, E. A. Duijnstee, O. El Tambouli, J. M. Ball, H. J. Snaith, J. Lim, and L. J. A. Koster, Revealing charge carrier mobility and defect densities in metal halide perovskites via space-charge-limited current measurements, ACS Energy Lett. **6**, 1087 (2021).

[125] L. M. Herz, Charge-carrier dynamics in organic-inorganic metal halide perovskites, Annu. Rev. Phys. Chem. **67**, 65 (2016).

[126] J. W. Rosenberg, M. J. Legodi, Y. Rakita, D. Cahen, and M. Diale, Laplace current deep level transient spectroscopy measurements of defect states in methylammonium lead bromide single crystals, J. Appl. Phys. **122**, 145701 (2017).

[127] S. Reichert, Q. An, Y.-W. Woo, A. Walsh, Y. Vaynzof, and C. Deibel, Probing the ionic defect landscape in halide perovskite solar cells, Nat. Commun. **11**, 6098 (2020).